Injected fluid volume controls seismicity migration in earthquake swarms through aseismic crack propagation

Philippe Danré[1], Dmitry Garagash[2], Louis De Barros[1], Frédéric Cappa[1], Jean-Paul Ampuero[1]

[1] Université Côte d'Azur, CNRS, Observatoire de la Côte d'Azur, IRD, Géoazur, 250 rue Albert Einstein, Sophia Antipolis 06560 Valbonne, France

[2] Dalhousie University, Department of Civil and Resource Engineering, Halifax, Canada

Key points :

- We show that induced seismicity migration depends on injected fluid volume
- Transient aseismic slip propagation along a fault explains the observed dependence
- Our results explain migration shape diversity and allow for accurate fluid volume reconstruction

Abstract

The evolution of fluid injection-induced seismicity, generally characterized through the number of events or their seismic moment, depends on, among other factors, the injected fluid volume. Migration of seismicity is observed during those sequences and might be caused by a range of mechanisms: fluid pressure diffusion, fluid-induced aseismic slip propagating along a stimulated fault, interactions between earthquakes. Recent theoretical and observational developments underline the important effect on seismicity migration of structural parameters, like fault criticality, or injection parameters, like flow rate or pressurization rate. Here, we analyze two well-studied injection-induced seismic sequences at the Soultz-sous-Fôret and Basel geothermal sites, and find that the evolution of the seismicity front distance primarily depends on the injected fluid volume. Based on a fracture mechanics model, we develop new equations relating seismicity migration to injected fluid volume and frictional and structural properties of the fault. We find that the propagation of a fluid-induced aseismic slip front along the stimulated fault, triggering seismicity, explains well the observations made on the two sequences. This model allows us to constrain parameters describing the seismicity front evolution and explains the diversity of migration patterns observed in injection-induced and natural earthquake swarms.

Plain language summary

Injection of fluids at depth may induce earthquakes, which can represent a hazard both for reservoir activities and populations. The magnitude and number of earthquakes correlate, at first order, with the injected fluid volume. Induced seismicity has also been observed to migrate away from the injection area, with a diversity of velocities and patterns. Migration has been attributed to several mechanisms like pore pressure diffusion, earthquake interactions or aseismic slip propagation. Here, we combine recent theoretical and observational developments to propose a new model to explain the migration of seismicity in two well-studied induced sequences in France and Switzerland. Our model directly relates migration distance to injected fluid volume, frictional parameters and structural properties of the fault. This generic model explains seismicity propagation and provides constraints on the relevant physical parameters controlling it. Applying this approach to natural fluid-induced earthquake swarms, we reconstruct fluid circulation dynamics during those sequences.

1. Introduction

1.1 Fluid circulation induces seismic and aseismic deformation

Earthquake swarms are sequences of clustered seismicity, with hundreds or thousands of events occurring over the course of days to years. Contrary to mainshock-aftershock sequences, swarms do not start with an event of magnitude far greater than the subsequent ones. Swarms can either be due to fluid injection at depth, for instance for geothermal reservoir development or wastewater storage (Kwiatek et al., 2019; Goebel et al., 2016), or occur naturally, such as in rift zones (De Barros et al., 2020), subduction zones (Vallée et al., 2013) or transform faults (Lohman and McGuire, 2007; Roland and McGuire, 2009). Fluid circulation seems to be the prominent driver for induced swarms and most of the natural swarms; indeed, fluid circulation is directly observed in anthropogenic injections at depth, and inferred in natural swarms given their depth, fracture density and geological context (Kraft et al., 2006; Horalek and Fischer, 2008; Shelly et al., 2013; Ruhl et al., 2016; Ross and Cochran, 2021).

Studying the relation between fluid circulation and seismicity is of particular interest as it is a pillar of risk management during anthropogenic injections. Globally, it is well established that maximum and cumulative seismic moments, as well as number of events, are related to the total injected volume for anthropogenic injections (McGarr, 1976; McGarr and Barbour, 2018; Van der Elst, 2016), while recent work showed that cumulative moment depends on injected volume through the whole injection duration (Bentz et al., 2020). Mitigating the impact of fluid injection on seismicity is crucial to prevent the occurrence of hazardous shaking, like during the M_w=5.5 Pohang earthquake attributed to a nearby fluid injection (Shapiro et al., 2021). For instance, close monitoring experiment in the vicinity of a densely populated area near Helsinki, Finland, successfully prevented the occurrence of M_w >1.9 earthquakes during a 47 days long fluid injection at kilometers depth (Kwiatek et al., 2019) despite the 18000 m^3 of injected fluids in a geothermal well.

While fluid injection may directly induce seismic slip, recent developments showed that it also leads to aseismic deformation. Field experiments in an underground facility showed that fluid-induced deformation was initially aseismic, then followed by seismicity (Guglielmi et al., 2015). At a smaller scale, laboratory experiments showed that a significant part of the deformation following an injection is aseismic (Goodfellow et al., 2015). Similar observations have been made in association with anthropogenic injections at depth; for example, a swarm in the Brawley, California geothermal field in 2012 was preceded and likely triggered by an aseismic slip transient (Wei et al., 2015), while hydraulic fracturing injections in northwestern Canada led to two major slow slip episodes not accompanied by significant seismic events (Eyre et al., 2022). Numerical modeling also showed that fluid injection can trigger aseismic transients, which in turn can trigger seismicity (Eyre et al., 2019; Wynants-Morel et al., 2020; Wang and Dunham, 2022).

Aseismic slip has also been observed in natural swarms. A swarm occurring in the Malawi rift, where fluid circulation can be expected given the geological context, was accompanied by significant aseismic slip (Hamiel et al., 2012). Recently, seismicity migration patterns in a swarm in California and geodetic and remote sensing data revealed the importance of aseismic slip in the onset of seismic activity (Sirorattanakul et al., 2022). However, the depth, low deformation and long duration of natural swarms make the observation and quantification of aseismic transients difficult. Despite that, similarities between global datasets of swarms and creep episodes supports that aseismic slip could be present in all swarms in various geological contexts associated with fluid circulation (Danré et al., 2022b). Effective stress drop values indeed suggest that during earthquake swarms, aseismic slip takes place in between discrete asperities slipping seismically (Fischer and Hainzl, 2017; Fischer and Hainzl, 2021; Danré et al., 2022b). Similarities in the scaling laws of swarms and slow slip events show that swarm migration velocity behaves like the rupture velocity of an aseismic slip transient (Danré et al., 2022b).

Therefore, while there is a strong link between fluid circulation and seismicity, recent and well documented developments showed that fluid-induced deformation might first be aseismic, and that

earthquakes could then be triggered by the stress perturbation caused by the aseismic slip transient. leading to the observed earthquake migration patterns during swarms.

1.2 Earthquake swarm migration as a witness of aseismic slip propagation

One of the most remarkable features of earthquake swarms is the migration of seismicity. It has been indeed observed, during injection-induced and natural swarms, that hypocenters propagate away from the first events or from the injection point (Danré et al., 2022b). Their migration velocity ranges from a few meters per day, like for the Cahuilla swarm (Ross et al., 2020), to a kilometer per day, as observed during the Rittershoffen induced sequence (Lengliné et al., 2014). Their migration duration ranges from a few hours to several years (Danré et al., 2022b).

Several mechanisms have been proposed to explain the migration of seismicity. It could directly result from pore pressure diffusion along a permeable fault. The increase in fluid pressure at the borehole in injection-induced sequences causes the diffusion of the pressure perturbation, leading to a decrease in the effective normal stress and fault strength, which triggers seismicity (Shapiro et al., 1997). The seismicity front, generally defined as the external envelope of migrating hypocenters (Goebel and Brodsky, 2018; Danré et al., 2022b), would then equal the pore pressure diffusion front and exhibit a square-root-like shape in a distance versus time plot, characteristic of the diffusion process. Conventionally, fitting this front evolution with a diffusion model provides an estimate of the hydraulic diffusivity of the fault zone, and a constraint on the fault permeability (Shapiro et al., 1997). The widespread study of seismicity fronts for injection-induced (Shapiro et al., 1997; Goebel and Brodsky, 2018) and natural earthquake swarms (Parotidis et al., 2005; Chen et al., 2012; Shelly et al., 2013) within this framework led to the idea that pore pressure diffusion is the most common mechanism responsible for earthquake migration.

While the hydraulic diffusion model is the most widely used framework to study swarm migration, several observations have highlighted its limitations and the potential importance of other mechanisms. Indeed, diffusivities inferred from seismicity migration are usually much higher than the hydraulic diffusivities obtained in laboratory and field experiments (Doan et al., 2006). Moreover, the square root behavior of seismicity fronts is not universal. Goebel and Brodsky (2018) identified two populations of migration behaviors in a global dataset of injection-induced sequences: one population has square root front shapes, interpreted as fluid diffusion on weakly coupled faults, and the other has linear fronts (constant migration speed), attributed to poroelastic processes on highly coupled faults. Moreover, Shu et al. (2023) obtained a scaling compatible with pore pressure diffusion, during laboratory experiments that do not involve fluids. De Barros et al. (2020) and other studies (Hatch et al., 2020; Fischer and Hainzl, 2021) also showed that different migration patterns can be observed at different scales during individual swarms: the overall migration over the whole swarm duration can be punctuated by numerous shorter and faster bursts. The migrating front shape is also sometimes more complex than a simple square root, as it is controlled by the fault stress state and criticality (ratio of initial shear stress to strength, Buijze et al., 2019 De Barros et al., 2021) while seismicity evolution also depends on injection history (volume and pressure, Almakari et al., 2019). These factors also control swarm migration in numerical and theoretical models (Wynants-Morel et al., 2020; Garagash, 2021; Saez and Lecampion, 2022). Finally, seismic slip can also occur ahead of the pressure diffusion front, through shear stress transfer from an aseismic slip transient along the fault, as highlighted in analytical and numerical modeling (Garagash and Germanovich, 2012; Bhattacharya and Viesca, 2019; Eyre et al., 2019; Wynants-Morel et al., 2020; Cappa et al., 2022) or during injection experiments (Guglielmi et al., 2015; Cappa et al, 2019).

Alternatively to a fluid pressure diffusion model, as aseismic deformation takes place during swarms (see section 1.1), seismicity can be triggered by shear stress perturbations caused by aseismic slip, in a similar way as repeating earthquakes are triggered by the surrounding aseismic slip (Uchida, 2019). This is confirmed by numerical modeling that showed that fluid-induced aseismic slip propagation

along a slip-weakening fault can trigger seismicity near the edges of the slipping zone (Wynants-Morel et al., 2020), and that aseismic slip on a velocity-strengthening fault can trigger seismicity on velocity-weakening patches (Chen and Lapusta, 2009; Eyre et al., 2019; Dublanchet and De Barros, 2021).

If aseismic slip is a dominant driver of earthquake swarm migration, rather than fluid pressure diffusion, migration characteristics should depend on injection history and mechanical fault parameters such as frictional properties. However, a complete model based on the numerous observations and theoretical results discussed above is still missing. Here, based on the migration evolution during two well-studied induced sequences, at the Soultz-sous-Fôret and Basel geothermal sites, and on the theoretical work of Garagash (2021) on fracture mechanics of rate-and-state faults during injection, we propose a new theoretical framework to model the triggering of seismicity by fluid-induced aseismic slip propagation that explains earthquake swarm migration shape and its diversity among sequences. We develop a theoretical relation between seismicity front distance and injected fluid volume, in which the relevant frictional and structural parameters are readily identified. We show how this relation can explain both individual migrations and the global behavior of earthquake swarms.

2. Empirical relation between seismicity migration and injection history

2.1 Data used in this study

We analyze the seismicity migration dynamics of two earthquake sequences induced by fluid injection in deep geothermal reservoirs that are well-studied and exhibit a simple injection history and seismicity.

The first sequence occurred in 1993 at the Soultz-sous-Forêts geothermal power plant in France. During the month of September, some 25900 m^3 of fluids were injected in the granitic basement at a depth of ~5 km over the course of ~18 days (Figure 1A). Subsequently, prolific seismicity occurred, involving thousands of events, although with very moderate magnitude, the largest event having magnitude M_w=0.8 (EOST & GEIE EMC., 2017; CSMA; Bourouis and Bernard, 2007). The observed seismic moment was much smaller than expected based on the injected volume and the empirical relation of McGarr (2014). This difference can be attributed to substantial aseismic slip occurring over the whole seismicity area during the injection, as indicated by borehole deformation measurements, repeating earthquakes (Bourouis and Bernard, 2007; Cauchie et al., 2020) and the seismogenic index value associated with the earthquake sequence (Danré et al., 2022a).

The second sequence took place under the city of Basel, Switzerland, in 2006. It followed the injection of ~11500 m^3 of fluids during ~5 days (Figure 1C). Because of the energetic seismicity, the injection activities were stopped prematurely. Despite this measure, a M_w=3.1 earthquake occurred a few hours after shut-in (Deichmann and Giardini, 2009; Herrmann et al., 2019), making this sequence one of the most characteristic case studies for risk mitigation during anthropogenic injections at depth. Passive monitoring imaged an aseismic transient induced by the injection (Hillers et al., 2015). This sequence shares common characteristics with other injection-induced swarms, mainly scaling laws (Danré et al., 2022a; Danré et al., 2022b), also suggesting that aseismic slip played a key role in its dynamics.

Both studied sequences are well documented in the literature and exhibit a simple injection history, comprising a continuous increase of flow rate (Figure 1), and a simple seismicity pattern. We consider for Basel that the delay between injection onset and the first event detected is negligible. The two sequences are end members of the injection-induced swarms family: the Soultz 1993 sequence has low magnitude seismicity, while the Basel one is the opposite (McGarr, 2014). For both sequences, the

seismicity is mainly localized along a 2D surface suggesting a reactivated fault plane (Danré et al., 2022b).

To study the migration evolution throughout each sequence, we define the seismicity front in the distance-time domain (so-called R-T plot). The origin distance is the median position of the 10 first events, and the origin time is the occurrence time of the first event (Figure 1 B,D). The seismicity front distance is defined as the 90th percentile of the event distances within non-overlapping sliding windows of 50 events. The corresponding time is defined as the time of the event located at the seismicity front distance.

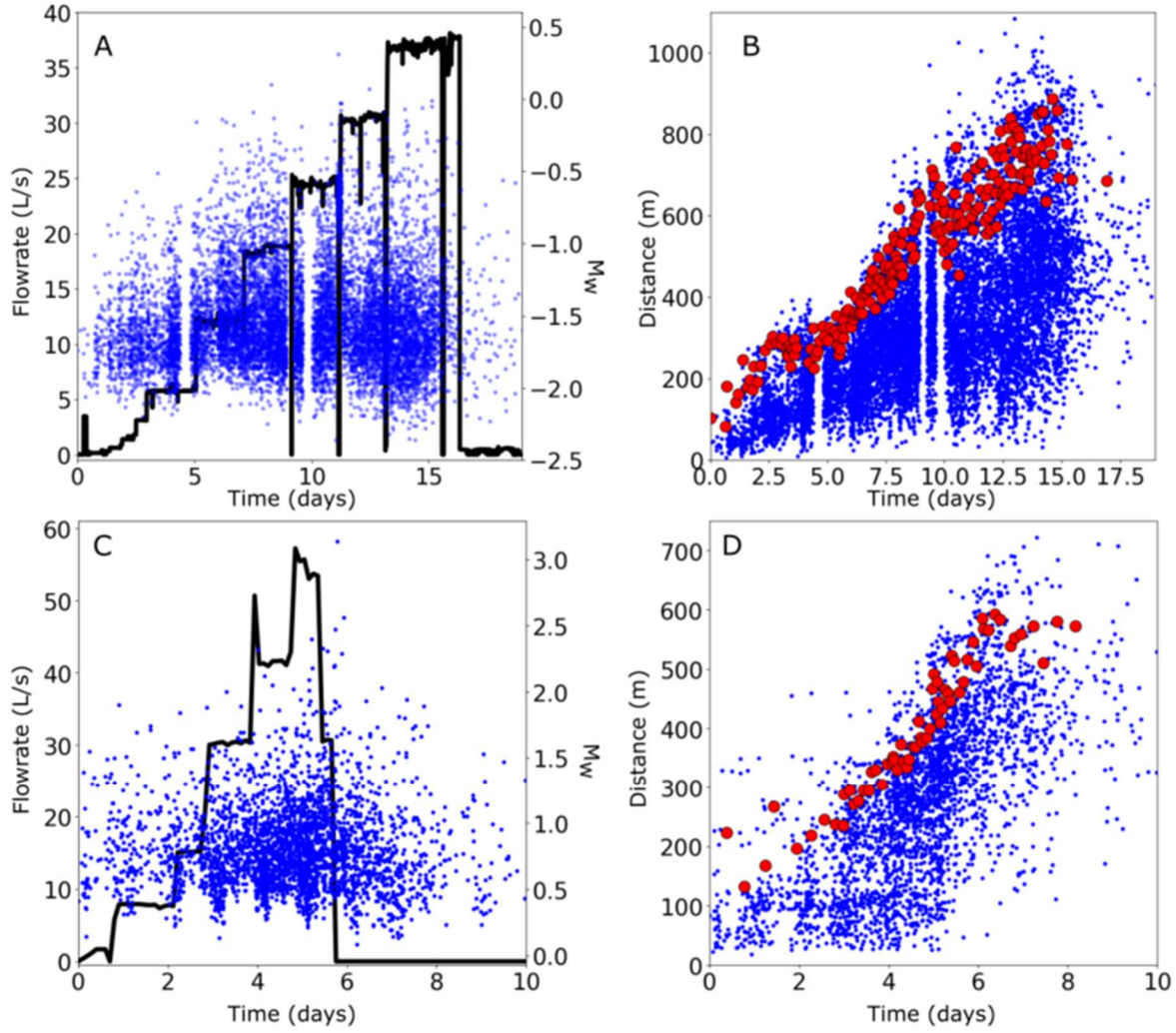

Figure 1. A: Temporal evolution of flow rate (black line) and magnitude (blue dots) for the 1993 Soultz-sous-Forêts sequence (EOST & GEIE EMC., 2017; CSMA). B: Distance as a function of occurrence time of all events (blue dots) and seismicity front (red dots). C and D: Same as A and B, respectively, but for the 2006 Basel injection (Herrman et al., 2019). Negative flow rates happening after injection arrest are not considered in this case (set to 0).

2.2 Injected fluid volume controls earthquake migration

As observed on a global dataset of injection-induced sequences, the earthquake migration duration is nearly equal to the injection duration (Danré et al., 2022a), highlighting the control of the seismic migration by the injection. In particular, we find that the spatial extent of seismicity is primarily controlled by the injected fluid volume, as revealed by plotting event distance as a function of the cumulative injected fluid volume (called hereafter R-V plot). As depicted in Figure 2, the seismicity front distance is well correlated with the square root of the cumulative injected volume, with correlation coefficients r^2=0.88 for Soultz 1993 and r^2=0.82 for Basel. The R-V best-fits are of slightly higher quality than the R-T fits by usual models like a square root model for pressure diffusion or a linear model (see Table 1). The dependence of migration distance on injected fluid volume does not imply a dependence on time, as the injection rate of the two sequences is not constant (Figure 1 A,C).

Name	**r^2 for fit in R-V**	r^2 for fit in R-T (diffusion)	r^2 for fit in R-T (linear)
Soultz 1993	**0.88**	0.82	0.86
Basel	**0.82**	0.77	0.79

Table 1 : Comparison between the r^2 values for fitting the seismicity front in the R-V domain (with a square root function) and in the R-t domain (with both a square root or a linear function) for Soultz 1993 and Basel.

We sum up this observation as :

$$R(t) = \sqrt{s_d V_{inj}(t)} \qquad (1)$$

Where R(t) is the seismicity front position at time t, $V_{inj}(t)$ the injected fluid volume at time t and s_d is a coefficient with dimensions of [m^{-1}]. We find similar values of s_d for both sequences: 24 m^{-1} for Basel and 26 m^{-1} for Soultz 1993.

Traditionally, injected fluid volume is thought to control seismic or total (seismic + aseismic) moment during induced earthquake swarms (McGarr, 2014; McGarr and Barbour, 2018; Danré et al., 2022a). The dependence observed in Figure 2 shows that the volume of injected fluids also controls the spatial extent of the seismicity.

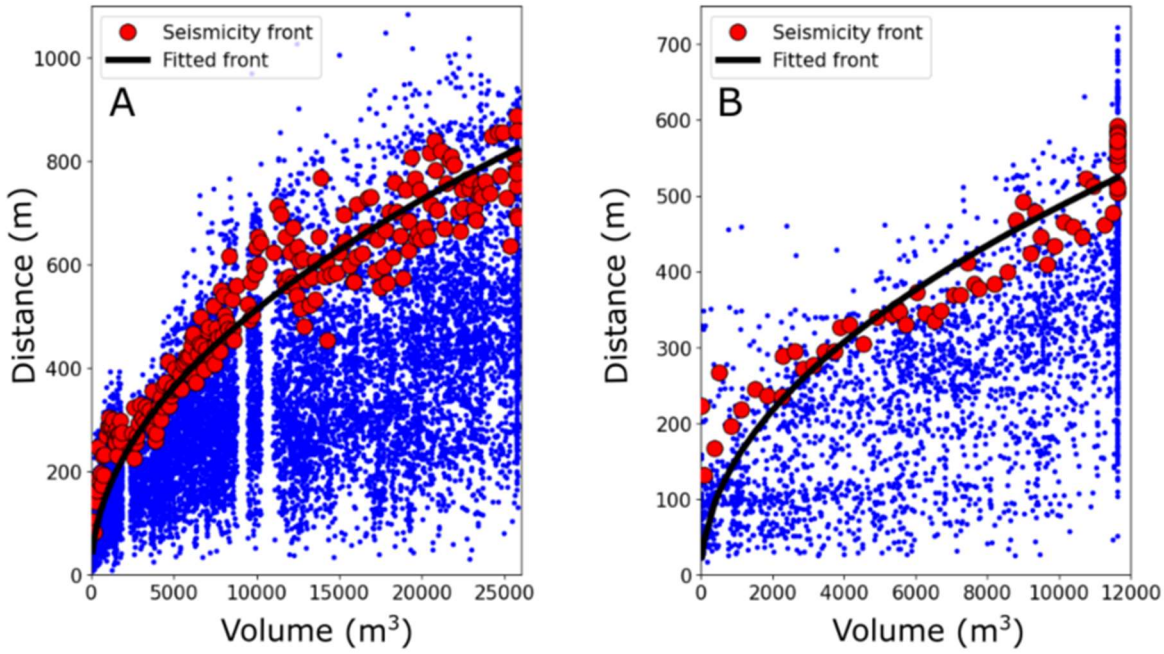

Figure 2. Evolution of seismicity front distance as a function of the cumulative injected fluid volume for the Soultz 1993 (A) and Basel (B) sequences. Blue dots indicate distance and volume of individual events. Red dots correspond to the seismicity front defined in the R-T domain. Black line is the best fitting square root model (Equation 1).

To explain the observed dependence of migration distance on injected volume and to relate this observation to mechanical parameters, we apply the fracture mechanics model of Garagash (2021) in the following section.

3. Aseismic crack propagation explains swarms behavior

3.1 Crack-like behavior of injection-induced sequences

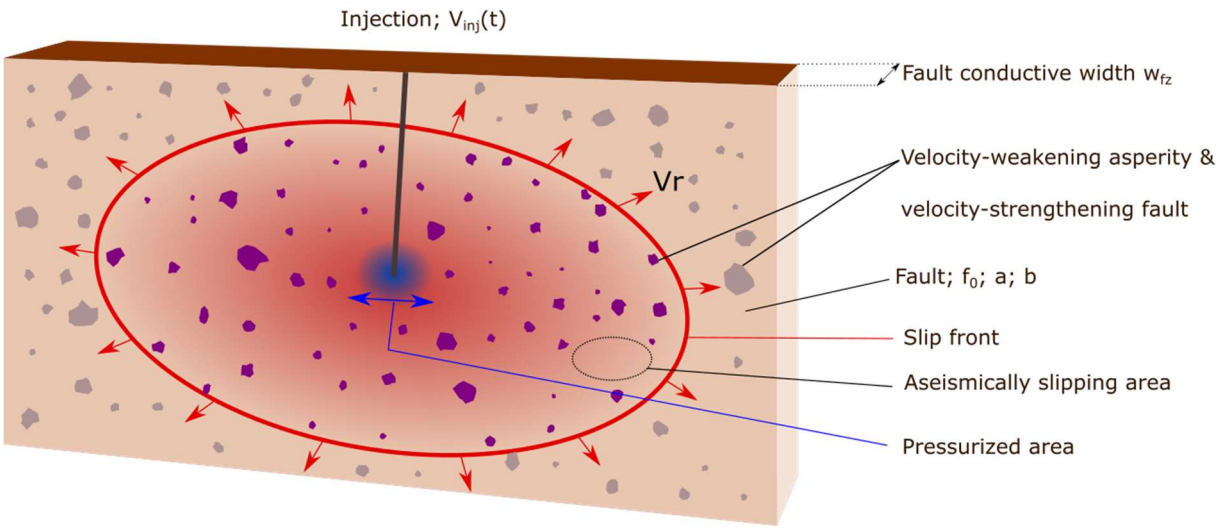

Figure 3. Schematic of the fault model considered. Along a single fault plane of conductive thickness w_{fz}, injection of fluids leads to pressure increase in a small expanding area (blue) which induces an expanding aseismic slip crack of much larger area (red). As the crack propagates, it triggers seismicity on asperities (polygons).

Let us consider a fault plane embedded in a 3D medium (Figure 3), governed by the rate-and-state friction law (Ruina, 1983) with velocity-strengthening properties and subject to homogeneous ambient stress. Fluid injection on the fault perturbs the pore pressure and hence the fault shear strength. This induces slow slip over the fault, which in turn triggers seismicity on discrete velocity-weakening asperities.

We treat the slow slip as a quasi-static crack and use fracture mechanics theory to model its evolution. The complete theoretical development of the model is presented in Appendix A. The stress drop within the crack is the sum of a uniform value $\Delta\tau$ and a contribution from the perturbations in pore pressure. When the slow slip zone outpaces the pressurized zone, the latter contribution can be represented by a net Coulomb point force, centered at the injection point, whose amplitude ΔT is the spatial integral over the fault of the reference friction coefficient f_0 times the pore pressure change. Assuming the pore pressure diffusion is confined within a narrow conductive zone surrounding the fault (blue area in figure 3), ΔT can be written as:

$$\Delta T(t) = \frac{f_0 V_{inj}(t)}{\beta\, w_{fz}} \qquad (2)$$

where β is the bulk pore compressibility parameter (e.g. Rice 2006) and w_{fz} the width of the conductive part of the fault zone (see Garagash (2021) and Table 2). We assume the conductive zone corresponds to the permeable part of the fault damage zone with an elevated fracture density.

A crack front equation of motion, assuming axisymmetric radial crack expansion, is established by expressing the stress intensity factor K of the crack as a function of its radius R (Equation A18; Garagash, 2021) :

$$K = \Delta\tau \sqrt{4R/\pi} + \frac{\Delta T}{(\pi R)^{3/2}} \qquad (3)$$

where

$$\Delta\tau = (b-a)\sigma_0 ln(\frac{V_s}{V_0}) \qquad (4)$$

where a and b are the rate-and-state friction coefficients, σ_0 the background effective normal stress, V_0 is the ambient fault slip velocity and V_s is the measure of the slip velocity within the transient crack, defined in Appendix A by Equations A14 and A15, assuming the fault is initially at steady state at $V = V_0$ and is not overstressed (Garagash, 2021). Here, because the fault is velocity-strengthening ($b - a < 0$), the effective stress drop $\Delta\tau$ is negative.

The crack propagation condition is $K = K_c$ where K_c is the fracture toughness, which depends on friction parameters and (weakly, logarithmically) on the crack front velocity (Garagash, 2021). This leads to

$$\Delta\tau + \frac{\Delta T}{2\pi R^2} = \frac{\sqrt{\pi} K_c}{2\sqrt{R}} \quad (5)$$

In Equation 5, the crack radius $R(t)$ depends on injection history through $\Delta T(t)$ and on different fault structural, frictional and initial parameters comprised in K_c and $\Delta\tau$ (Equations 5 and A17). When the toughness term can be neglected (Appendix A), Equation 5 becomes

$$\Delta\tau \quad + \frac{\Delta T}{2\pi R^2} = 0 \qquad (6)$$

Given the crack is loaded by a concentrated point force and a negative uniform stress drop, its slip profile decreases steeply as a function of distance to the crack center, approximately as the inverse of distance (Equation A22). Here we use this feature for a first-order consistency check of our model. For the studied sequences, the seismic moment density distributions (Figure 4) overall decrease as a function of distance to the origin in a similar manner at all times. Assuming that seismicity is triggered by the aseismic slip, and following similar observations of seismic asperities loaded by surrounding aseismic slip (Chen and Lapusta, 2009; Uchida, 2019), we further assume that the cumulative seismic moment is proportional to the aseismic slip, i.e. that the seismic to aseismic slip ratio is fixed. Under this framework, the seismic moment density distributions can be compared to the aseismic slip distribution predicted by the crack model (Figure 4): we find they are consistent in the range of distances where both decay, i.e. at distances >0.3 times the distance to the front. At shorter distances, the model overestimates the observationally-inferred seismic slip. The finite size of the fluid pressurized zone or an offset between the injection point and the fault, two ingredients absent from the model, would not produce lower aseismic slip at short distances. Catalog location errors are also unlikely to induce a bias of this form. We interpret this mismatch as indicating that the seismic to aseismic slip ratio is not uniform, but lower near the injection point. One possible reason for that is the occurrence of fault opening, i.e. loss of contact between the fault walls, due to overpressure, but the injection pressures in these sequences are not large enough to produce fault opening. A more likely possibility is that seismic ruptures are hampered by an increase of the earthquake nucleation size caused by higher pore fluid pressure there: theoretical estimates of the initiation size of seismic ruptures (e.g. Rubin and Ampuero, 2005) are inversely proportional to effective normal stress. A pulse-like slip model would also produce a tail of decaying seismicity behind the front, but seems less relevant as seismicity would be located only in a narrow ring near the front, and since pulse behavior can be expected only after arrest of injection (Saez and Lecampion, 2022). We next apply the formulated crack model to our sequences, to test if it can explain quantitatively the observations.

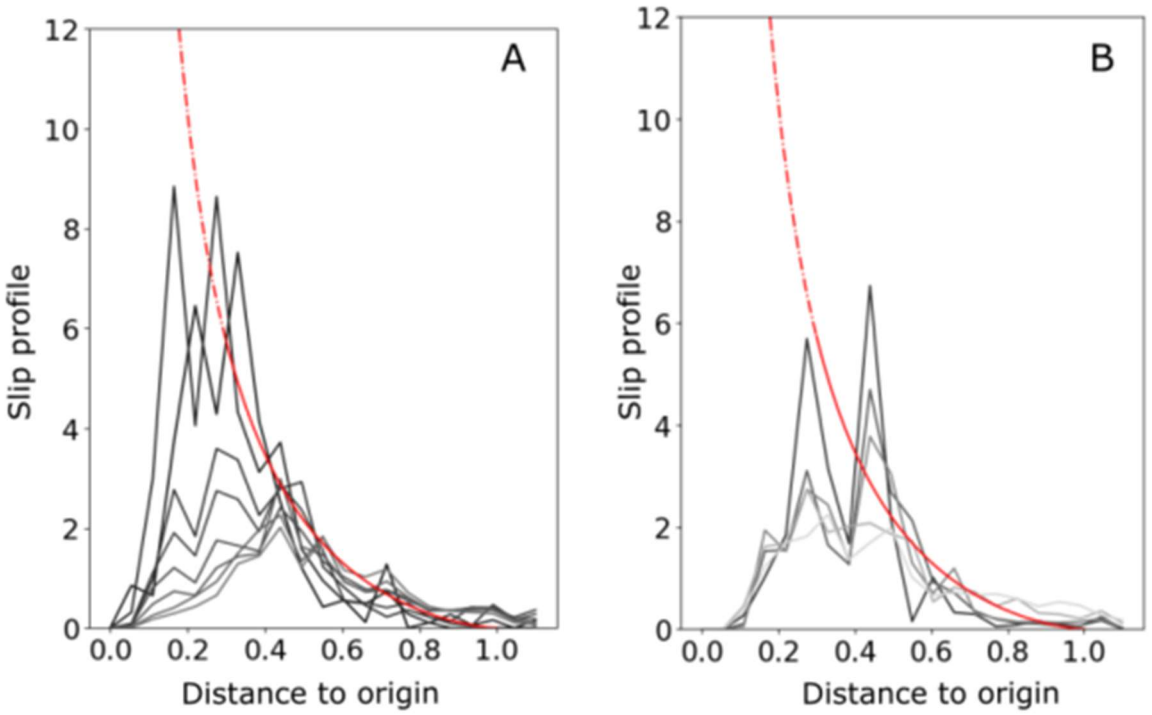

Figure 4. Comparison of the spatial distribution of seismic moment density observed in swarms with aseismic slip predicted by the crack model. The radial distributions for Soultz 1993 (A) and Basel (B) are shown at various times as a function of distance to the origin normalized by the distance to the seismicity front. For each radial bin, the seismic moment density is computed as the sum of the seismic moment of all events with hypocenters lying within the bin, divided by the bin area (a ring). It is then normalized by its average over the area between 0.3 and 1. The curves correspond to the moment computed while injection is occurring (while flow rate is positive) on expanding time windows incremented by 2 days over the first 16 days for Soultz and by 1 day over the first 5 days for Basel (greyscale getting darker with time). The red line represents the theoretical slip profile of the circular crack model loaded by a point pressure (Equation A22), divided by its average slip between normalized distances 0.3 and 1 (and dashed line corresponds to theory below 0.3)

3.2 Observed volume dependence of the seismicity front explained by the migration of a fluid-induced aseismic transient

Equation 5 describes the temporal evolution of the seismicity front distance $R(t)$, assuming earthquakes are triggered by a propagating aseismic slip. Typical orders of magnitude of the parameters involved, taken from the literature, are listed in Table 2. Based on those values and on the injection history of the Soultz 1993 and Basel sequences, we plot on Figure 5 the expected temporal evolution of the three terms involved in Equation 5. To estimate $\Delta\tau$, we compute an order of magnitude of slip velocity following Garagash (2021) and Equation A17. A precise estimate of V_s is not necessary given the logarithmic dependence in Equation 4.

When distance increases, the toughness term in Equation 5 can be neglected compared to the other two terms (Figure 5), leading to the following approximate equation for the front propagation, equivalent to the zero toughness approximation (Equation 6) :

$$\Delta\tau \quad + \frac{\Delta T(t)}{2\pi\, R(t)^2} \sim 0 \quad \Leftrightarrow \quad R(t) = \sqrt{\frac{-\Delta T(t)}{2\pi\, \Delta\tau}} \qquad (7)$$

with $\Delta\tau$ <0 (see 4.1). As $\Delta T(t)$ is directly proportional to the injected volume (Equation 2), the distance $R(t)$ is found to depend on the square root of $V_{inj}(t)$, as shown by the observations (Equation 1). Therefore, the constant s_d derived from the observations (Figure 2 and Equation 1) when fitting the seismicity front as a function of the injected volume can be related to physical parameters using Equation 6 as:

$$s_d = -\frac{f_0}{2\pi\, \beta\, w_{fz} \Delta\tau} \qquad (8)$$

Name	Meaning	Value	Reference(s)
f_0	Coefficient of friction	0.6	
β	Compressibility	$10^{-10}\ Pa^{-1}$	
w_{fz}	Fault zone width	~10 m	Genter et al., 2000; Ziegler and Evans, 2020
a	Friction law coefficient	0.014	
b	Friction law coefficient	0.01	
σ_0	Effective normal stress	100 MPa	
V_s	Slip velocity	$\sim 10^{-8}\ m.s^{-1}$	See Equation A17
V_0	Ambient slip velocity	$\sim 0.1\ mm/year$	Buchmann and Connolly, 2007
K_c	Fault toughness	20 MPa$\sqrt{m}$	See Appendix

Table 2 : Typical values of model parameters.

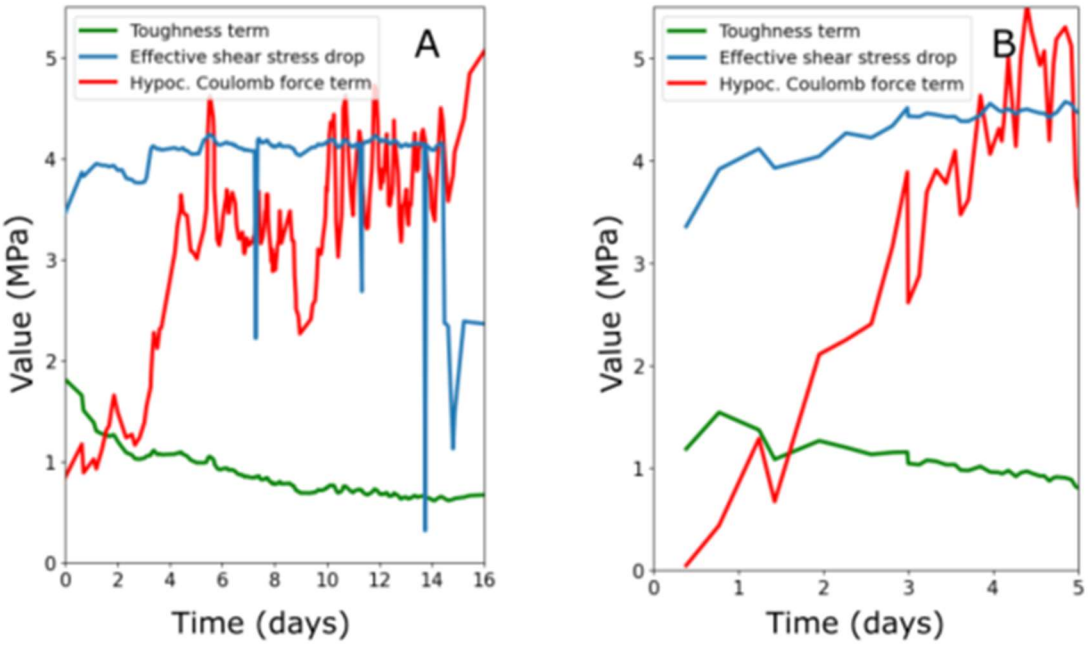

Figure 5. Temporal evolution of the different terms of Equation 5 : the toughness term, the effective shear stress drop and the hypocentral Coulomb force term, assuming values for the involved parameters from Table 2. A – For Soultz 1993. B – For Basel.

We can then use the volume history $V_{inj}(t)$ to reconstruct the front evolution as a function of time (Equation 1, Figures 2 and 6). The model therefore allows reconstructing the R-T front with a greater temporal complexity than usual diffusion or linear migration models. Indeed, our reconstruction leads to a non-constant migration velocity and to an arrest of the propagation when the injection stops. It also accounts for the injection history as expected from recent theoretical studies (Garagash, 2021; Saez and Lecampion, 2022).

The seismicity front position at the beginning of injection (t<4 days for Soultz 1993 or t<2 days for Basel) is not very well reconstructed. This misfit might be due to failure of the assumption that the K_c term is negligible at early stages (Figures 5). Solving the full equation of motion (Equation 5) leads to a relation between seismicity front distance and injected volume more complex than a simple square root, but precise determination of K_c would require knowledge of other parameter values as well (Appendix A). Another explanation might be that the offset corresponds to the physical distance between the injection point and the seismogenic fault, a few tenth of meters in the case of Basel (Deichmann and Giardini, 2009), or to the fact that injection is done on an open-hole section rather than at a single point (Deichman and Giardini, 2009; Cauchie et al., 2020).

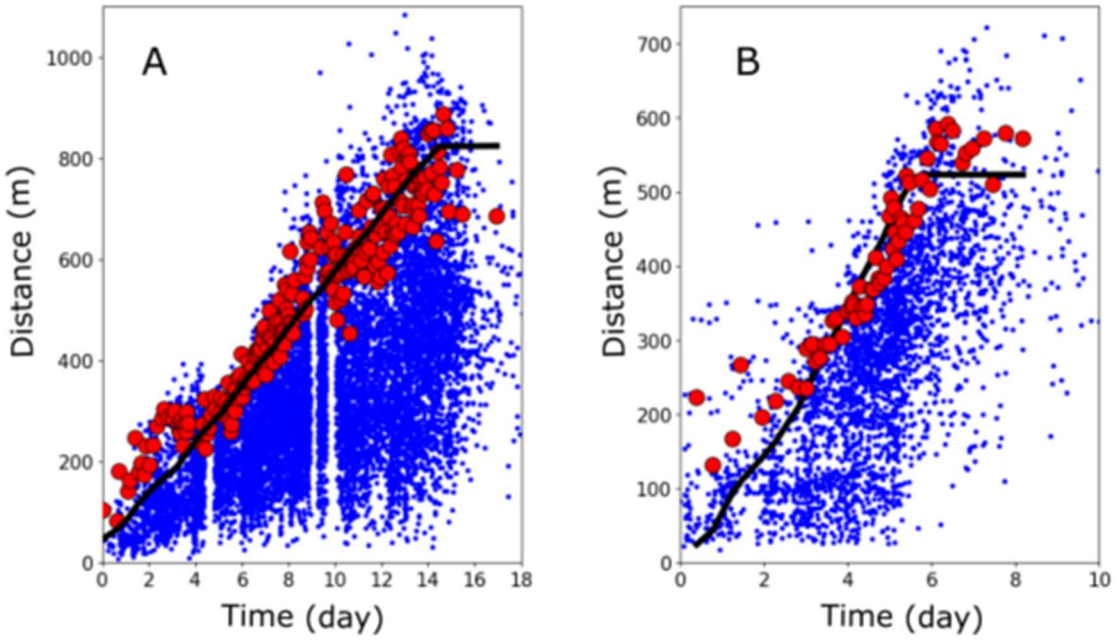

Figure 6. Seismicity front distance as a function of time (red dots) and its reconstruction based on the distance vs volume fitting obtained from Figure 2 (black line), over the whole sequence duration. Blue dots are individual events.

3.3 Migration shape diversity explained through variability in injection dynamics

A direct consequence of Equation 6 is that the seismicity migration shape in the R-T domain could serve to constrain the temporal evolution of injected volume during earthquake swarms, for which injection history is not known. Indeed, as presented in Figure 7, a square root R-T migration implies a

constant flow rate and a linearly increasing volume, while a linear migration implies a linearly increasing flow rate. This can provide an explanation to the observed diversity of migration shapes in induced swarms (e.g. Goebel and Brodsky, 2018). The flow rate during the Basel injection can be considered at first order linear (Figure 1C), which would explain the apparent linear migration of seismicity observed (Figure 1D). For Soultz 1993, the flow rate history is more complex, with incremental steps, which should lead to a more complex migration shape in between the constant and linear flow rate cases (Figures 1A,B and 7). This might explain why the front shape is closer to a square root shape in Soultz 1993 than in Basel. According to our model (Equation 6), the shape of the slip front also depends on several parameters like fault frictional and hydraulic parameters, stress state, compressibility and fault zone width.

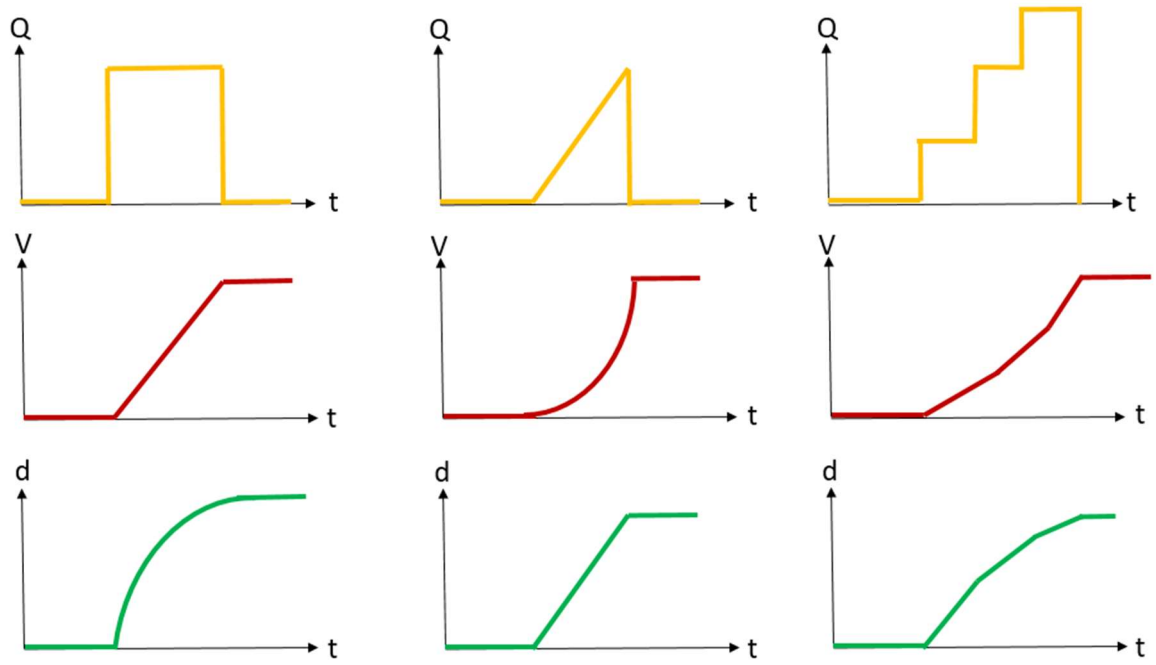

Figure 7. Simple cases illustrating the relation between flow rate and volume histories and seismicity front shape in the R-T domain, for two cases: (left) a constant flow rate, (middle) a linear flow rate and (right) a stepwise increasing flow rate.

4. Discussion

4.1 Apparent velocity-strengthening regime occurrence in swarms

A direct consequence of Equation 6 is that $\Delta\tau$ should be negative, which implies that the friction regime should be velocity-strengthening (a-b>0 in Equation 5) for all cases. Following Equation 5 for the zero-toughness limit, we indeed have :

$$\Delta\tau = -\frac{\Delta T(t)}{2\pi\, d(t)^2} \qquad (9)$$

For the two sequences studied here, if we consider the final values of distance and injected fluid volumes, and parameters from Table 2, we get shear stress drops values $\Delta\tau$ ~ -5 MPa for both sequences. These stress drop values are consistent with the theoretical value of -3 MPa obtained from Equation 4 considering the values of (a-b), σ_0, V_s and V_0 in Table 2.

The limited magnitude of seismicity observed during swarms suggests that swarm seismicity might indeed occur on isolated velocity-weakening asperities embedded on a velocity-strengthening fault, even if seismicity could still happen without such asperities (Wynants-Morel et al., 2020). If the fault was globally velocity-weakening, large fault-spanning seismicity would be more prevalent. A velocity-strengthening regime seems consistent with in situ observations, as friction coefficient was found to increase during a well-studied fluid injection field experiment (Guglielmi et al., 2015), and such a behavior is thought to be one possible cause for the aseismic transient measured. Velocity strengthening behavior has also been characterized in laboratory experiments on granite samples, in conditions similar to the ones expected at geothermal reservoir depth (Zhang et al., 2022). Velocity-strengthening behavior could be explained by mineralization processes: minerals like chlorite favor velocity-strengthening, while others like epidote lead to velocity-weakening (An et al., 2021, Zhang et al., 2022). For instance, in Basel, chlorite is expected to be present in the minerals along the fault, among others (Alt-Epping et al., 2013). Faults in sedimentary cover are also more likely to be rate-strengthening due to the presence of clay and organic content (Kohli and Zoback, 2011). In addition to mineralization, parameters like temperature, pore fluid pressure, fluid temperature, fault maturity, etc. are expected to contribute to the friction regime (Cappa et al., 2019; Ji et al., 2022). However, investigating those is far beyond the scope of this work as we focus on proposing a simple but effective model to explain observations.

Wang and Dunham (2022) successfully reconstructed the seismicity observed during fluid injection in the Cooper Basin, Australia, using a numerical model that assumes a velocity-strengthening fault, explained by the potential presence of phyllosilicates in the fault zone. For the Soultz 1993 sequence, the presence of repeating events, asperity interactions, slip rate decay suggest that the observed seismicity is due to a combined effect of velocity-weakening on seismic asperities embedded in a velocity-strengthening matrix (Figure 3, Bourouis and Bernard, 2007). Such a behavior has also been investigated through numerical modeling (Chen and Lapusta, 2009; Dublanchet and De Barros, 2021) which showed that a velocity-strengthening fault creeping can load velocity weakening asperities, leading to seismic events.

The results obtained might also be valid in a velocity-weakening fault that is understressed, i.e. whose shear stress before injection is below the frictional steady state at ambient conditions, Δf_0<0. Indeed, our results lead to $\Delta\tau \quad < 0$, which, on a slightly understressed fault, can still be compatible with a negative value of (a-b) (see Appendix). However, to underline the duality between the propagating aseismic slip and the triggered seismicity occurring on discrete patches, we prefer to consider the fault as an apparent velocity-strengthening surface with velocity-weakening asperities hosting seismic events.

Earthquake swarms also present other interesting features in their distribution of seismic moment release over the seismicity area (Fischer and Hainzl, 2017; Danré et al., 2022b), which highlight the presence and importance of aseismic slip behind the seismicity front. Induced sequences also present very distinct seismogenic responses to an injection (in terms of number of events or magnitudes), studied through the seismogenic index (Shapiro et al., 2010). In this work, we did not study either what happens behind the seismicity front or the released moments, but only focus on its propagation. Other mechanisms like earthquake interactions or direct triggering through fluid pressure perturbation might also take place behind the seismicity front and play a role in the global moment release, explaining the variety of behaviors observed in swarms. Our work is also limited by the fact that we considered seismicity to be triggered instantly by the aseismic transient, while in reality triggering could involve a delay.

As suggested by observations (De Barros et al., 2021) and theory (Garagash, 2021; Saez and Lecampion, 2022), frictional properties and stress state might need to be taken into account to describe swarm migration through a parameter like criticality, defined as the ratio of initial shear stress and

strength in Wynants-Morel et al. (2020). In our model, such parameters are involved (Equation 6). Further constraining them might also help understand why the seismic response of the Soultz 1993 sequence is less energetic than the Basel one, despite similar injected fluid volumes. More generally, our model may provide a generic explanation to the observed diversity of seismogenic responses (in terms of moment, number of events or migration behavior) to fluid injections in nature and during anthropogenic activities (Shapiro et al., 2010; McGarr, 2014; McGarr and Barbour, 2018; Danré et al., 2022a).

4.2 Investigating global migration features of swarms

The propagation model developed in this work can be reasonably expected to apply to fluid-induced earthquake swarms in general. Indeed, based on scaling relations, many natural and injection-induced earthquake swarms, including the two sequences studied here, have similar characteristics (Danré et al., 2022b).

If we assume that, at first order, injected volume V_{inj} grows linearly with time t, with a constant flow rate Q and an injection duration T, we get from Equations 1 and 6 :

$$V_{rupt} = T^{-0.5} \sqrt{\frac{-f_0 Q}{2\pi\beta w_{fz}\Delta\tau}} = T^{-0.5} \sqrt{s_d Q} \qquad (10)$$

Assuming that, over the wide range of durations, migration distances and injected fluid volumes of injection-induced swarms, flow rate is similar from one injection to another, typically between 10 and 50 L/s, then Equation 10 implies that migration velocity of injection-induced swarms should scale with their duration with an exponent of n=-0.5. Flow rates for natural earthquake swarms were also observed to be similar (Danré et al. 2022a), so the same scaling relation should apply to natural swarms as well. Therefore, the model developed in this work seems to offer a generic explanation for both individual migration evolution in swarms and global scaling laws observed through the study of large datasets.

Indeed, Danré et al. (2022b) observed that $V_{rupt} \propto T^{-0.55}$ for a wide range of injection-induced and natural earthquake swarms. By applying Equation 10 to the best fitting line on their dataset, assuming Q=10 L/s, we get an average estimate of s_d=139 m^{-1}. For Q=50 L/s, we get s_d=28 m^{-1}. Assuming f_0, β and w_{fz} values as in Table 2, following Equation 8 we get average values of $\Delta\tau = -0.7$ MPa for Q=10 L/s and $\Delta\tau = -3.4$ MPa for Q=50 L/s. This shows that constraining the parameters involved in Equations 4 and 6 might help constrain other parameters, like a-b, through the determination of s_d for each sequence.

4.3 Swarm migration as a proxy for injection dynamics

The correlation found between seismicity front distance R and injected fluid volume V_{inj} implies that R can be used to constrain the injected volume shape, through the relation $V_{inj} \propto R^2$ (Equation 7). This is of particular interest when injected volume is not known, which is the case for natural fluid-induced earthquake swarms. Indeed, those sequences are thought to be driven by the same processes as injection-induced swarms since they share many similar characteristics (Danré et al., 2022b). Recent efforts aimed at estimating the total amount of fluids circulating during some natural earthquake swarms (Danré et al., 2022a, Mukuhira et al., 2022). Danré et al. (2022a) proposed a precise way to quantify the total fluid volume circulating, once the swarm is finished. We propose here a way to combine this approach with the observation made of $V_{inj} \propto R^2$ in order to fully constrain the injected fluid volume. The squared seismicity front distance evolution gives the injected volume $V_{inj}(t)$ shape, while the final value of injected volume constrained through the statistical analysis of Danré et al. (2022a) gives its amplitude.

For Soultz 1993 and Basel, we compared the squared seismic front distance R^2, put to scale with the total injected volume, with the actual $V_{inj}(t)$ (Figure 8). We find that our volume reconstruction reproduces quite well the injected volume evolution with time (as indirectly observed in Figure 2). The discrepancies could be explained by the relative scatter of seismicity front positions, even though the two curves match pretty well. Beyond injection-induced swarms, for comparison we use the same approach to reconstruct the injected volume as a function of time, using the final injected fluid volume estimated in Danré et al. (2022a) as calibration, for two well studied natural earthquake swarms, the 2015 Gulf of Corinth swarm and the 2016-2020 Cahuilla swarm (De Barros et al., 2020; Ross et al., 2020). Those two sequences have similar global scaling laws as Basel and Soultz 1993 (Danré et al., 2022b). Figure 8 shows the resulting estimate $V_{inj}(t)$ as a function of time. For Corinth 2015, the flow rate seems quite constant as volume increases linearly, while for the Cahuilla swarm the injection seems to accelerate with time. Taking distances of R=600 m and R=3500 m for Corinth 2015 and Cahuilla respectively (Danré et al., 2022b), and estimated volume values of 5100 m^3 and 1,3.10^6 m^3 (Danré et al., 2022a) leads to s_d estimates of s_d =70 m^{-1} and s_d =9 $m^{-1}$for the two sequences respectively. Therefore, it seems possible to combine our observations of $V_{inj} \propto R^2$ and already existing methods of final volume estimation to better constrain the temporal injection dynamics occurring during fluid-induced swarms. For instance, the linear migration of seismicity during the 2015 Corinth swarm (De Barros et al., 2020) suggests that the fluid source responsible for the observed deformation presents a linear evolution of the flow rate.

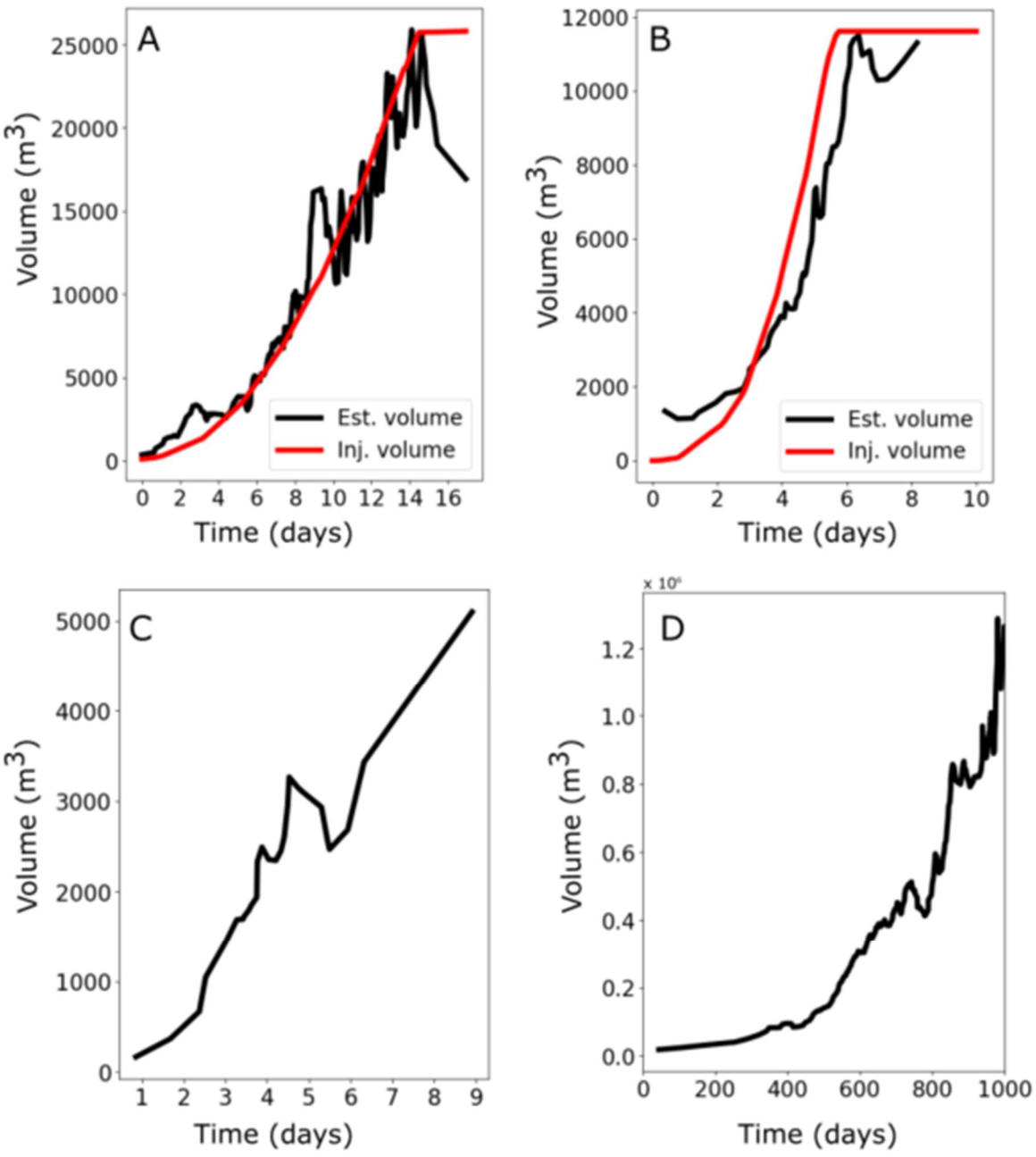

Figure 8. Injected volume (red) and estimated volume (black), in cubic meters, as a function of time for Soultz 1993 (A) and Basel (B). Estimated volumes for the 2015 Corinth swarm (De Barros et al., 2020; C) and the 2016-2020 Cahuilla swarm (Ross et al., 2020; D).

Conclusion

We studied the seismicity front propagation during two well-studied injection-induced earthquake sequences in geothermal reservoirs. We find from the seismological and hydraulic observations that the evolution of the seismicity front distance is strongly correlated to the square root of the injected

fluid volume. Based on this new relation between distance and volume, we introduced a new geometrical parameter, s_d, to accurately explain the volume dependence of seismicity migration. Interestingly, we found a similar value of s_d for the two cases studied here, regardless of their specific site characteristics, highlighting a possible generic macroscopic behavior. Moreover, we showed that a model of fluid-induced aseismic crack propagating along a hydraulically conductive, rate-and-state fault explains the observations made on the two sequences studied as well as global scaling relations for swarms. Our result suggests that faults hosting swarms during fluid injection behave with an apparent velocity-strengthening frictional behavior, a regime that favors aseismic slip propagation. This allows us to infer other physical parameters involved in the relation between distance and volume, like the effective shear stress drop. Independent constraints on the structural model parameters, like the stress state, conductive fault width or rock compressibility, could allow estimating better the frictional properties that control slip transients along fluid-stimulated faults, thus potentially improving upon the classic scaling of induced earthquake magnitude with injected fluid volume.

Data availability statement

Data for the Soultz fluid injections are available on the CDGP web services (https://cdgp.u-strasbg.fr/). Data for the Basel sequence is available in Herrman et al., 2019.

Acknowledgments

This work was partly supported by the ANR INSeis under contract ANR-22-CE49-0018. DG and JPA were supported by the French government through the UCAJEDI Investments-in-the-Future project (ANR-15-IDEX-01) managed by the National Research Agency (ANR).

Appendix A : Mechanical framework

Here we develop analytical solutions for the slip distribution, moment release and energy release rate of a circular shear crack loaded by a point force located at its center $\Delta T \delta_{Dirac}(x, y)$ plus a colinear uniform stress drop $\Delta\tau$. We consider an analogue, approximately equivalent tensile circular crack formulation (see, e.g., Galis et al., 2017; Ripperger et al., 2007). By assuming a rate-and-state frictional fault and applying a suitable crack front equation of motion (Garagash, 2021), we derive a relation between crack growth and loading.

Consider a crack of radius R in the (x,y) plane loaded by a uniform stress drop $\Delta\tau = \tau_0 - \tau$, where $\tau = \sigma_{zx}$ and $\tau_0 = {\sigma_{zx}}^0$ are actual and initial shear stresses in the x-direction on the crack plane, plus a point force ΔT acting in the x-direction and located at the crack center. The point force is a simplified representation of the load induced by fluid injection and pressure diffusion. This approximation is expected to be adequate when the pressurized zone is substantially smaller than the induced crack.

The resulting slip distribution is the sum of the slip induced by each of these two loading contributions:

$$\delta = \delta_{\Delta\tau} + \delta_{\Delta T} \qquad \text{(Equation A1)}$$

The corresponding components of slip in the collinear (x) and normal (y) directions to the loading direction, taken from e.g. Tada et al. (2000) for the uniform stress drop and from Fabrikant (1989) for the central force, are:

$$\delta_{\Delta\tau,x} = \frac{1-\nu}{1-\frac{\nu}{2}} \frac{\Delta\tau R}{\mu} \frac{4}{\pi} \sqrt{1-\rho^2}$$

$$\delta_{\Delta\tau,y} = 0$$

$$\delta_{\Delta T,x} = \frac{\Delta T}{\mu R} \frac{2}{\pi^2} \left[\left(1 - \nu \ sin^2(\Phi)\right) \left(\sqrt{1-\rho^2} + \frac{arccos\ (\rho)}{\rho} \right) - \frac{1-\nu+\nu^2}{1-\nu/2} \sqrt{1-\rho^2} \right]$$

$$\delta_{\Delta T,y} = \frac{\Delta T}{\mu R} \frac{\nu}{\pi^2} \left(\sqrt{1-\rho^2} + \frac{arccos\ (\rho)}{\rho} \right) sin(2\Phi)$$

where $\rho = r/R$ is the normalized radial position and Φ is the polar angle (defined such that Φ=0 corresponds to the x-direction).

The released moment is:

$$M = \mu \int_{crack} \quad \delta dS = \frac{1-\nu}{1-\frac{\nu}{2}} \left(\frac{8}{3} \Delta\tau R^3 + \frac{4}{\pi} \Delta T R \right) \quad \text{(Equation A2)}$$

Note that slip in the y-direction does not contribute to the moment: owing to its symmetries, its integral is exactly zero.

Our analysis of the crack evolution relies on fracture mechanics, with additional simplifying assumptions that render the problem more tractable analytically and thus amenable to gain further insight. Based on the corresponding in-plane K_{II} and anti-plane K_{III} stress intensity factors as function of position (angle Φ) along the circular crack front (Tada et al., 2000; Fabrikant 1989), we evaluate its front-averaged energy release rate:

$$G = \frac{1}{2\pi} \int_0^{2\pi} \quad \left[\frac{1-\nu}{2\mu} K_{II}^2(\Phi) + \frac{1}{2\mu} K_{III}^2(\Phi) \right] d\Phi = \frac{1-\nu}{2\mu\left(1-\frac{\nu}{2}\right)} \left[\left(\frac{2}{\pi} \Delta\tau \sqrt{\pi R} + \frac{\Delta T}{(\pi R)^{\frac{3}{2}}} \right)^2 + \frac{\nu^2}{1-\nu} \frac{\Delta T^2}{(\pi R)^3} \right] \quad \text{(Equation A3)}$$

We consider a simplified description borrowed from a tensile (mode I) crack formulation, which has been previously used to estimate the energy release rate of a circular shear crack (Galis et al., 2017; Ripperger et al., 2007). For a tensile crack, the crack opening is axisymmetric:

$$\delta_I = \frac{1-\nu}{\mu_I} \left(\Delta\tau\ R \frac{4}{\pi} \sqrt{1-\rho^2} + \frac{\Delta T}{R} \frac{2}{\pi^2} \frac{arccos(\rho)}{\rho} \right) \qquad \text{(Equation A4)}$$

where $\mu_I = \mu$ for an actual tensile crack, but is understood here as an equivalent modulus for a shear crack that we define below. The corresponding released moment is

$$M_I = \frac{(1-\nu)\mu}{\mu_I} \left(\frac{8}{3} \Delta\tau R^3 + \frac{4}{\pi} \Delta T R \right) \qquad \text{(Equation A5)}$$

and the energy release rate is

$$G_I = \frac{1-\nu}{2\mu_I} \left(\frac{2}{\pi} \Delta\tau \sqrt{\pi R} + \frac{\Delta T}{(\pi R)^{\frac{3}{2}}} \right)^2 \qquad \text{(Equation A6)}$$

We observe that the true moment M (Equation A2) and the tensile analog moment M_I (Equation A5) are identical if the equivalent modulus is defined as

$$\mu_I = \mu(1-\nu/2) \qquad \text{(Equation A7)}$$

Similarly, we find that the front-averaged energy release rate G for the shear crack (Equation A3) and for the tensile analog (Equation A6 using Equation A7) differ by the second term in Equation A3. The

relative weight of this term, $\frac{\nu^2}{1-\nu}$, has typical values much smaller than 1 and thus generally can be considered small. In the following, we adopt the analog tensile crack with equivalent modulus $\mu_I = \mu(1-\frac{\nu}{2})$ to approximate a shear crack and its equation of motion. We will also use hereafter the notation $\mu_I' = \mu\frac{1-\nu/2}{1-\nu}$.

The equation of motion (EofM) for the equivalent tensile crack model stems from the energy flux balance around the rupture front $G_I = G_c$, where G_c is the fault fracture energy and G_I the energy release rate given by Equation A6. It is convenient to re-express the EofM in the form of the stress intensity factor matching an analogue fault toughness K_c,

$$\frac{2}{\pi}\Delta\tau\sqrt{\pi R} + \frac{\Delta T}{(\pi R)^{3/2}} = K_c \qquad \text{with} \qquad K_c = \sqrt{2\mu_I' G_c} \quad \text{(Equation A8)}$$

We now specialize the above EofM, in particular the fault toughness and the stress drop, for the case of a rate- and state- dependent fault friction, following the approach of Garagash (2021). Fault friction f is composed of a rate-dependent direct effect and a state-dependent effect (Rice, 1983), where the rate of change of state θ with slip is a function of the friction departure from its steady-state value $f_{ss}(V)$, and particularized here for the so-called 'slip law' (Ruina, 1983) :

$$f = f_0 + a\, ln\left(\frac{V}{V_0}\right) + \theta \qquad \text{and} \qquad \frac{d\theta}{d\delta} = -\frac{f - f_{ss}(V)}{L} \quad \text{(Equation A9)}$$

where L is the characteristic state-evolution slip distance, $f_0 = \tau_0/\sigma_0$ the prestress ratio and V_0 the ambient fault slip rate. The steady-state friction is expressed in reference to the fault ambient state as

$$f_{ss}(V) = f_0 - \Delta f_0 + (a-b)\, ln\left(\frac{V}{V_0}\right) \qquad \text{(Equation A10)}$$

where $\Delta f_0 = f_0 - f_{ss}(V_0)$ is the initial value of the fault over/under stress-ratio.
Garagash (2021) studied the fracture energy G_c expended at the front of a slip transient propagating with velocity v_r on a rate-and-state fault. His approximate equations (2.12) and (2.20) in the case of aseismic slip give

$$G_c \approx [\Delta f_0 + b\, ln\,(\tfrac{v_r}{v_0})]\sigma_0 L \qquad \text{(Equation A11)}$$

This is a function of the variable v_r and of constants representing the ambient state on the fault: σ_0, Δf_0, and the characteristic rupture speed $v_0 = \mu_I' V_0/(b\sigma_0)$. This informs the expression for toughness K_c in the EofM (A8).

To estimate the stress drop, first, we approximate the shear stress in the 'bulk' of the crack, i.e. away from the crack front, by the steady-state strength, $\tau \approx \tau_{ss}(V) = f_{ss}(V)\sigma_0$, which generally varies along the crack since V does. Second, we treat the spatially uniform background stress drop $\Delta\tau$ in the EofM as an 'effective' measure of the actual, spatially varying stress drop, $\tau_0 - \tau_{ss}(V)$, retrieved by matching the corresponding expressions for the stress intensity factors :

$$K_{\Delta\tau} = \frac{2}{\sqrt{\pi R}}\int_0^R [\tau_0 - \tau_{ss}(V)]\frac{r dr}{\sqrt{R^2 - r^2}} = \frac{2}{\pi}\Delta\tau\sqrt{\pi R} \qquad \text{(Equation A12)}$$

The slip rate distribution $V(r)$ is obtained by differentiating in time the slip solution (Equation A4) and expressing it as a function of normalized distance $\rho = r/R(t)$:

$$V = V_I(\rho) = \frac{2v_r}{\mu_I'\sqrt{\pi R}}\left[\frac{K_c}{\sqrt{1-\rho^2}} + \frac{\Delta\dot{T}}{\pi v_r\sqrt{\pi R}}\frac{arccos(\rho)}{\rho}\right] \qquad \text{(Equation A13)}$$

where $\Delta\dot{T} = \frac{d(\Delta T)}{dt}$ is the rate of hypocentral force. In deriving the above expression, we used the time derivative of the EofM and assumed negligible rates of the stress drop and toughness compared to the

rate of hypocentral force. Equation (A12) can then be used to express the effective stress drop $\Delta\tau$ in terms of an effective slip rate V_s defined by

$$\Delta\tau = (f_0 - f_{ss}(V_s))\sigma_0 \quad \text{with} \quad f_{ss}(V_s) \equiv \int_0^1 f_{ss}(V_I(\rho))\frac{\rho d\rho}{\sqrt{1-\rho^2}} \qquad \text{(Equation A14)}$$

Substituting (A13) for V_I in (A14) and rearranging, we obtain the effective slip rate

$$V_s = \frac{\Delta\dot{T}}{\mu_I' R}\mathrm{V}(K) \quad \text{with} \quad \mathrm{V}(K) = \frac{2}{\pi^2} exp(\int_0^1 ln[\frac{K}{\sqrt{1-\rho^2}} + \frac{arccos(\rho)}{\rho}]\frac{\rho d\rho}{\sqrt{1-\rho^2}}) \qquad \text{(Equation A15)}$$

where K is the dimensionless toughness parameter defined by

$$K = \frac{\pi v_r \sqrt{\pi R} K_c}{\Delta\dot{T}} \qquad \text{(Equation A16)}$$

The function $\mathrm{V}(K)$ describes the dependence of the normalized effective slip rate on the normalized toughness. End-member cases of zero and large toughness can be worked out analytically: $\mathrm{V}(0) = (2\pi)^{-1} exp\left(1 - Si\left(\frac{\pi}{2}\right)\right) \sim 0.110$ and $\mathrm{V}(K \gg 1) \approx \left(\frac{2}{\pi^2}\right)K$. The corresponding asymptotic expression for the dimensional slip rate when $K_c = 0$ is :

$$V_s^{(K_c=0)} = 0.110 \times \frac{\Delta\dot{T}}{\mu_I' R} \qquad \text{(Equation A17)}$$

In summary, upon substitution of (A14) and (A10), the EofM (A8) is

$$\frac{2}{\pi}\left[\Delta f_0 - (a-b)\, ln\left(\frac{V_s}{V_0}\right)\right]\sigma_0\sqrt{\pi R} + \frac{\Delta T}{(\pi R)^{3/2}} = K_c \qquad \text{with} \quad K_c = \sqrt{2\mu_I' G_c(v_r)} \quad \text{(Equation A18)}$$

Together with expressions (A15-A16) and (A11) for V_s and $G_c(v_r)$, respectively, (A18) constitutes a relation between crack front position $R(t)$, crack front speed $v_r = dR/dt$ and hypocentral force $\Delta T(t)$ that is an ordinary differential equation for the crack front position $R(t)$.

Let us consider the limiting solution where the effect of the fault toughness K_c is negligible. Under this condition, the EofM yields

$$R^{(K_c=0)} = \sqrt{-\frac{\Delta T}{2\pi\Delta\tau}} \qquad \text{with} \quad \Delta\tau = [\Delta f_0 - (a-b)\, ln(0.110 \times \frac{\Delta\dot{T}}{\mu_I' R V_0})]\sigma_0 \qquad \text{(Equation A19)}$$

This solution exists when the stress drop is negative ($\Delta\tau < 0$), i.e. when there is stress increase along the slipping patch. This is realized, for example, when the fault is rate-strengthening ($a - b > 0$) and is initially at steady-state ($\Delta f_0 = 0$). Although, this is the case mostly alluded to in the main text, the zero-toughness aseismic slip transient solution also exists on a rate-weakening fault ($a - b < 0$), provided that the fault is initially sufficiently under-stressed ($\Delta f_0 < 0$) so that $\Delta\tau < 0$.

Strictly speaking, Equation A19 is implicit due to the dependence of the stress drop on R. However this dependence is weak (logarithmic) and stress drop can be treated as approximately constant over a range R of interest. The front speed of the zero-toughness transient is approximately

$$v_r^{(K_c=0)} \approx \frac{\Delta\dot{T}}{2\sqrt{-2\pi\Delta\tau\Delta T}} \qquad \text{(Equation A20)}$$

The solution (A19-A20) can be used to estimate the consistency of the underlying zero toughness assumption by evaluating the dimensionless toughness (A16) :

$$K = 0.702 \times \frac{K_c}{(-\Delta\tau\Delta T)^{1/4}} \qquad \text{(Equation A21)}$$

The numerical prefactor is $(\pi^3/128)^{1/4}$.

Once the front position is solved, the distribution of slip follows from (A4) when substituting the expression for $\Delta\tau$ resulting from the EofM :

$$\delta(\rho) = \frac{\Delta T}{R\mu_I'}\frac{2}{\pi^2}\left(\frac{arccos(\rho)}{\rho} - \sqrt{1-\rho^2}\right) \qquad \text{(Equation A22)}$$

Taking elastic parameters $\mu = 30$ GPa and $\nu = 0.25$, an approximate constant flowrate of Q=10 L/s, and estimates of f_0, β, w_{fz} as in Table 2 of the main text, we get an estimate of $V_s^{(K_c=0)}$ following Equation A17, leading to $V_s^{(K_c=0)} \sim 10^{-8} m.s^{-1}$. Values of $a = 0.014$ and $b = 0.01$ then lead to an estimate of $\Delta\tau \sim -3$ MPa when taking the V_0 estimate of Table 2 and following Equation A19 with $\Delta f_0 = 0$. Using the same estimates, we get from Equation A11 :

$$G_c = 1000 \times \frac{L}{1\ [mm]}\ [Pa.m]$$

and $K_c = \sqrt{2\mu_I' G_c} \approx 7\ \left[MPa\sqrt{m}\right] \times \sqrt{\frac{L}{1\ [mm]}}$. The state evolution slip distance L is considered here to vary from 0.03 to 10 mm, reflecting possibly variable fault maturity/size. This suggests ranges of G_c from 30 to 10^4 Pa.m and K_c from about 1 to 22 MPa$\sqrt{m}$.

To validate the zero-toughness assumption adopted for the aseismic slip modeling in the main text, we estimate the dimensionless toughness based on the zero-toughness solution (A21) with $\Delta\tau \sim -3$ MPa, an injected volume $V_{inj} \sim 10^4\ m^3$ and other constants from Table 2. This leads to K values indeed small, varying between 0.01 and 0.16 for L between 0.03 and 10 mm.

References

Almakari, M., Dublanchet, P., Chauris, H., & Pellet, F. (2019). Effect of the injection scenario on the rate and magnitude content of injection-induced seismicity: Case of a heterogeneous fault. *Journal of Geophysical Research: Solid Earth*, *124*(8), 8426-8448.

Alt-Epping, P., Diamond, L. W., Häring, M. O., Ladner, F., & Meier, D. B. (2013). Prediction of water–rock interaction and porosity evolution in a granitoid-hosted enhanced geothermal system, using constraints from the 5 km Basel-1 well. *Applied Geochemistry*, *38*, 121-133.

An, M., Zhang, F., Min, K. B., Elsworth, D., Marone, C., & He, C. (2021). The Potential for Low-Grade Metamorphism to Facilitate Fault Instability in a Geothermal Reservoir. *Geophysical Research Letters*, *48*(11), e2021GL093552.

Bentz, S., Kwiatek, G., Martínez-Garzón, P., Bohnhoff, M., & Dresen, G. (2020). Seismic moment evolution during hydraulic stimulations. *Geophysical Research Letters*, *47*(5), e2019GL086185.

Bhattacharya, P., & Viesca, R. C. (2019). Fluid-induced aseismic fault slip outpaces pore-fluid migration. *Science*, *364*(6439), 464-468.

Bourouis, S., & Bernard, P. (2007). Evidence for coupled seismic and aseismic fault slip during water injection in the geothermal site of Soultz (France), and implications for seismogenic transients. *Geophysical Journal International*, *169*(2), 723-732.

Buchmann, T. J., & Connolly, P. T. (2007). Contemporary kinematics of the Upper Rhine Graben: A 3D finite element approach. *Global and Planetary Change*, *58*(1-4), 287-309.

Buijze, L., P. A. J. Van den Bogert, B. B. T. Wassing, & B. Orlic (2019). Nucleation and arrest of dynamic rupture induced by reservoir depletion. *Journal of Geophysical Research: Solid Earth*, 124(4), 3620-3645.

Cappa, F., Scuderi, M. M., Collettini, C., Guglielmi, Y., & Avouac, J. P. (2019). Stabilization of fault slip by fluid injection in the laboratory and in situ. *Science advances*, *5*(3), eaau4065.

Cappa, F., Guglielmi, Y., Nussbaum, C., De Barros, L., & Birkholzer, J. (2022). Fluid migration in low-permeability faults driven by decoupling of fault slip and opening. *Nature Geoscience*, *15*(9), 747-751.

Cauchie, L., Lengliné, O., & Schmittbuhl, J. (2020). Seismic asperity size evolution during fluid injection: case study of the 1993 Soultz-sous-Forêts injection. *Geophysical Journal International*, *221*(2), 968-980.

Chen, T., & Lapusta, N. (2009). Scaling of small repeating earthquakes explained by interaction of seismic and aseismic slip in a rate and state fault model. *Journal of Geophysical Research: Solid Earth*, *114*(B1).

Chen, X., Shearer, P. M., & Abercrombie, R. E. (2012). Spatial migration of earthquakes within seismic clusters in Southern California: Evidence for fluid diffusion. *Journal of Geophysical Research: Solid Earth*, *117*(B4).

Danré, P., De Barros, L., & Cappa, F. (2022). Inferring fluid volume during earthquake swarms using seismic catalogues. *Geophysical Journal International*, *232*(2), 829-841.

Danré, P., De Barros, L., Cappa, F., & Ampuero, J. P. (2022). Prevalence of aseismic slip linking fluid injection to natural and anthropogenic seismic swarms. *Journal of Geophysical Research: Solid Earth*, e2022JB025571.

De Barros, L., Cappa, F., Deschamps, A., & Dublanchet, P. (2020). Imbricated aseismic slip and fluid diffusion drive a seismic swarm in the Corinth Gulf, Greece. *Geophysical Research Letters*, *47*(9), e2020GL087142.

De Barros, L., Wynants-Morel, N., Cappa, F., & Danré, P. (2021). Migration of Fluid-Induced Seismicity Reveals the Seismogenic State of Faults. *Journal of Geophysical Research: Solid Earth*, *126*(11), e2021JB022767.

Deichmann, N., & Giardini, D. (2009). Earthquakes induced by the stimulation of an enhanced geothermal system below Basel (Switzerland). *Seismological Research Letters*, *80*(5), 784-798.

Doan, M. L., Brodsky, E. E., Kano, Y., & Ma, K. F. (2006). In situ measurement of the hydraulic diffusivity of the active Chelungpu Fault, Taiwan. *Geophysical Research Letters*, *33*(16).

Dublanchet, P., & De Barros, L. (2021). Dual seismic migration velocities in seismic swarms. *Geophysical Research Letters*, *48*(1), e2020GL090025.

EOST & GEIE EMC, 2017. Episode: 1993 stimulation Soultz-sous-Forêts [Collection]. EOST - CDGP. https://doi.org/10.25577/SSFS1993

Eyre, T. S., Eaton, D. W., Garagash, D. I., Zecevic, M., Venieri, M., Weir, R., & Lawton, D. C. (2019). The role of aseismic slip in hydraulic fracturing–induced seismicity. *Science advances*, *5*(8), eaav7172.

Eyre, T. S., Samsonov, S., Feng, W., Kao, H., & Eaton, D. W. (2022). InSAR data reveal that the largest hydraulic fracturing-induced earthquake in Canada, to date, is a slow-slip event. *Scientific reports*, *12*(1), 1-12.

Fabrikant, V. (1989). *Applications of potential theory in mechanics: a selection of new results* (Vol. 51). Dordrecht; Boston: Kluwer Academic Publishers.

Fischer, T., & Hainzl, S. (2017). Effective stress drop of earthquake clusters. *Bulletin of the Seismological Society of America*, *107*(5), 2247-2257.

Fischer, T., & Hainzl, S. (2021). The growth of earthquake clusters. *Frontiers in Earth Science*, *9*, 638336.

Galis, M., Ampuero, J. P., Mai, P. M., & Cappa, F. (2017). Induced seismicity provides insight into why earthquake ruptures stop. *Science advances*, *3*(12), eaap7528.

Garagash, D. I., & Germanovich, L. N. (2012). Nucleation and arrest of dynamic slip on a pressurized fault. *Journal of Geophysical Research: Solid Earth*, *117*(B10).

Garagash, D. I. (2021). Fracture mechanics of rate-and-state faults and fluid injection induced slip. *Philosophical Transactions of the Royal Society A*, *379*(2196), 20200129.

Genter, A., Traineau, H., Ledésert, B., Bourgine, B., & Gentier, S. (2000, May). Over 10 years of geological investigations within the HDR Soultz project, France. In *World Geothermal Congress* (Vol. 2000). Reykjavik, Iceland: Int. Geotherm. Assoc..

Goebel, T. H., Hosseini, S. M., Cappa, F., Hauksson, E., Ampuero, J. P., Aminzadeh, F., & Saleeby, J. B. (2016). Wastewater disposal and earthquake swarm activity at the southern end of the Central Valley, California. *Geophysical Research Letters*, *43*(3), 1092-1099.

Goebel, T. H., & Brodsky, E. E. (2018). The spatial footprint of injection wells in a global compilation of induced earthquake sequences. *Science*, *361*(6405), 899-904.

Goodfellow, S. D., Nasseri, M. H. B., Maxwell, S. C., & Young, R. P. (2015). Hydraulic fracture energy budget: Insights from the laboratory. *Geophysical Research Letters*, *42*(9), 3179-3187.

Guglielmi, Y., Cappa, F., Avouac, J. P., Henry, P., & Elsworth, D. (2015). Seismicity triggered by fluid injection–induced aseismic slip. *Science*, *348*(6240), 1224-1226.

Hamiel, Y., Baer, G., Kalindekafe, L., Dombola, K., & Chindandali, P. (2012). Seismic and aseismic slip evolution and deformation associated with the 2009–2010 northern Malawi earthquake swarm, East African Rift. *Geophysical Journal International*, *191*(3), 898-908.

Hatch, R. L., Abercrombie, R. E., Ruhl, C. J., & Smith, K. D. (2020). Evidence of aseismic and fluid-driven processes in a small complex seismic swarm near Virginia City, Nevada. *Geophysical Research Letters*, *47*(4), e2019GL085477.

Herrmann, M., Kraft, T., Tormann, T., Scarabello, L., & Wiemer, S. (2019). A consistent high-resolution catalog of induced seismicity in Basel based on matched filter detection and tailored post-processing. *Journal of Geophysical Research: Solid Earth*, *124*(8), 8449-8477.

Hillers, G., Husen, S., Obermann, A., Planès, T., Larose, E., & Campillo, M. (2015). Noise-based monitoring and imaging of aseismic transient deformation induced by the 2006 Basel reservoir stimulationPassive monitoring of deformation. *Geophysics*, *80*(4), KS51-KS68.

Hirose, H., Matsuzawa, T., Kimura, T., & Kimura, H. (2014). The Boso slow slip events in 2007 and 2011 as a driving process for the accompanying earthquake swarm. *Geophysical Research Letters*, *41*(8), 2778-2785.

Horálek, J., & Fischer, T. (2008). Role of crustal fluids in triggering the West Bohemia/Vogtland earthquake swarms: just what we know (a review). *Studia Geophysica et Geodaetica*, *52*(4), 455-478.

Ji, Y., Hofmann, H., Duan, K., & Zang, A. (2022). Laboratory experiments on fault behavior towards better understanding of injection-induced seismicity in geoenergy systems. *Earth-Science Reviews*, *226*, 103916.

Kohli, A. H., & Zoback, M. D. (2011, December). Rate and State Frictional Properties of Shale Gas Reservoir Rocks and FIB/SEM Microscopy of Lab-Generated Fault Surfaces. In *AGU Fall Meeting Abstracts* (Vol. 2011, pp. T43C-2341).

Kraft, T., Wassermann, J., Schmedes, E., & Igel, H. (2006). Meteorological triggering of earthquake swarms at Mt. Hochstaufen, SE-Germany. *Tectonophysics*, *424*(3-4), 245-258.

Kwiatek, G., Saarno, T., Ader, T., Bluemle, F., Bohnhoff, M., Chendorain, M., ... & Wollin, C. (2019). Controlling fluid-induced seismicity during a 6.1-km-deep geothermal stimulation in Finland. *Science Advances*, *5*(5), eaav7224.

Lengliné, O., Lamourette, L., Vivin, L., Cuenot, N., & Schmittbuhl, J. (2014). Fluid-induced earthquakes with variable stress drop. *Journal of Geophysical Research: Solid Earth*, *119*(12), 8900-8913.

Lohman, R. B., & McGuire, J. J. (2007). Earthquake swarms driven by aseismic creep in the Salton Trough, California. *Journal of Geophysical Research: Solid Earth*, *112*(B4).

McGarr, A. (1976). Seismic moments and volume changes. *Journal of geophysical research*, *81*(8), 1487-1494.

McGarr, A. (2014). Maximum magnitude earthquakes induced by fluid injection. *Journal of Geophysical Research: solid earth*, *119*(2), 1008-1019.

McGarr, A., & Barbour, A. J. (2018). Injection-induced moment release can also be aseismic. *Geophysical Research Letters*, *45*(11), 5344-5351.

Mukuhira, Y., Uno, M., & Yoshida, K. (2022). Slab-derived fluid storage in the crust elucidated by earthquake swarm. *Communications Earth & Environment*, *3*(1), 1-7.

Parotidis, M., Shapiro, S. A., & Rothert, E. (2004). Back front of seismicity induced after termination of borehole fluid injection. *Geophysical research letters*, *31*(2).

Parotidis, M., Shapiro, S. A., & Rothert, E. (2005). Evidence for triggering of the Vogtland swarms 2000 by pore pressure diffusion. *Journal of Geophysical Research: Solid Earth*, *110*(B5).

Rice, J. R. (1985). Constitutive relations for fault slip and earthquake instabilities. *Instabilities in continuous media*, 443-475.

Rice, J.R. (2006). Heating and weakening of faults during earthquake slip. *Journal of Geophysical Research: Solid Earth*, *111*(B5).

Ripperger, J., Ampuero, J. P., Mai, P. M., & Giardini, D. (2007). Earthquake source characteristics from dynamic rupture with constrained stochastic fault stress. *Journal of Geophysical Research: Solid Earth*, *112*(B4).

Ruina, A. (1983). Slip instability and state variable friction laws. *Journal of Geophysical Research: Solid Earth*, *88*(B12), 10359-10370.

Roland, E., & McGuire, J. J. (2009). Earthquake swarms on transform faults. *Geophysical Journal International*, *178*(3), 1677-1690.

Ross, Z. E., Cochran, E. S., Trugman, D. T., & Smith, J. D. (2020). 3D fault architecture controls the dynamism of earthquake swarms. *Science*, *368*(6497), 1357-1361.

Ross, Z. E., & Cochran, E. S. (2021). Evidence for latent crustal fluid injection transients in Southern California from long-duration earthquake swarms. *Geophysical Research Letters*, *48*(12), e2021GL092465.

Rubin, A. M., & Ampuero, J. P. (2005). Earthquake nucleation on (aging) rate and state faults. *Journal of Geophysical Research: Solid Earth*, *110*(B11), B11312.

Ruhl, C. J., Abercrombie, R. E., Smith, K. D., & Zaliapin, I. (2016). Complex spatiotemporal evolution of the 2008 Mw 4.9 Mogul earthquake swarm (Reno, Nevada): Interplay of fluid and faulting. *Journal of Geophysical Research: Solid Earth*, *121*(11), 8196-8216.

Sáez, A., Lecampion, B., Bhattacharya, P., & Viesca, R. C. (2022). Three-dimensional fluid-driven stable frictional ruptures. *Journal of the Mechanics and Physics of Solids*, *160*, 104754.

Shapiro, S. A., Huenges, E., & Borm, G. (1997). Estimating the crust permeability from fluid-injection-induced seismic emission at the KTB site. *Geophysical Journal International*, *131*(2), F15-F18.

Shapiro, S. A., Rothert, E., Rath, V., & Rindschwentner, J. (2002). Characterization of fluid transport properties of reservoirs using induced microseismicity. *Geophysics*, *67*(1), 212-220.

Shapiro, S. A., Dinske, C., Langenbruch, C., & Wenzel, F. (2010). Seismogenic index and magnitude probability of earthquakes induced during reservoir fluid stimulations. *The Leading Edge*, *29*(3), 304-309.

Shapiro, S. A., Kim, K. H., & Ree, J. H. (2021). Magnitude and nucleation time of the 2017 Pohang Earthquake point to its predictable artificial triggering. *Nature communications*, *12*(1), 1-9.

Shelly, D. R., Hill, D. P., Massin, F., Farrell, J., Smith, R. B., & Taira, T. A. (2013). A fluid-driven earthquake swarm on the margin of the Yellowstone caldera. *Journal of Geophysical Research: Solid Earth*, *118*(9), 4872-4886.

Shu, W., Lengliné, O., & Schmittbuhl, J. (2023). *Collective behavior of asperities before large stick-slip events* (No. EGU23-4151). Copernicus Meetings.

Sirorattanakul, K., Ross, Z. E., Khoshmanesh, M., Cochran, E. S., Acosta, M., & Avouac, J. P. (2022). The 2020 Westmorland, California earthquake swarm as aftershocks of a slow slip event sustained by fluid flow. *Journal of Geophysical Research: Solid Earth*, e2022JB024693.

Tada, H. (2000). Stress analysis results for common test specimen configurations. *The stress analysis of cracks handbook*.

Uchida, N. (2019). Detection of repeating earthquakes and their application in characterizing slow fault slip. *Progress in Earth and Planetary Science*, *6*(1), 1-21.

Vallée, M., Nocquet, J. M., Battaglia, J., Font, Y., Segovia, M., Regnier, M., ... & Chlieh, M. (2013). Intense interface seismicity triggered by a shallow slow slip event in the Central Ecuador subduction zone. *Journal of Geophysical Research: Solid Earth*, *118*(6), 2965-2981.

Van der Elst, N. J., Page, M. T., Weiser, D. A., Goebel, T. H., & Hosseini, S. M. (2016). Induced earthquake magnitudes are as large as (statistically) expected. *Journal of Geophysical Research: Solid Earth*, *121*(6), 4575-4590.

Wang, T. A., & Dunham, E. M. (2022). Hindcasting injection-induced aseismic slip and microseismicity at the Cooper Basin Enhanced Geothermal Systems Project.

Wei, S., Avouac, J. P., Hudnut, K. W., Donnellan, A., Parker, J. W., Graves, R. W., ... & Eneva, M. (2015). The 2012 Brawley swarm triggered by injection-induced aseismic slip. *Earth and Planetary Science Letters*, *422*, 115-125.

Wynants-Morel, N., Cappa, F., De Barros, L., & Ampuero, J. P. (2020). Stress perturbation from aseismic slip drives the seismic front during fluid injection in a permeable fault. *Journal of Geophysical Research: Solid Earth*, *125*(7), e2019JB019179.

Zhang, F., Huang, R., An, M., Min, K. B., Elsworth, D., Hofmann, H., & Wang, X. (2022). Competing Controls of Effective Stress Variation and Chloritization on Friction and Stability of Faults in Granite: Implications for Seismicity Triggered by Fluid Injection. *Journal of Geophysical Research: Solid Earth*, *127*(8), e2022JB024310.

Ziegler, M., & Evans, K. F. (2020). Comparative study of Basel EGS reservoir faults inferred from analysis of microseismic cluster datasets with fracture zones obtained from well log analysis. *Journal of Structural Geology*, *130*, 103923.